



Article

Effect of Ga_2O_3 Addition on the Properties of Garnet-Type Ta-Doped $\text{Li}_7\text{La}_3\text{Zr}_2\text{O}_{12}$ Solid Electrolyte

Yusuke Yamazaki, Shotaro Miyake, Keigo Akimoto and Ryoji Inada *

Department of Electrical and Electronic Information Engineering, Toyohashi University of Technology, Toyohashi 4418580, Aichi, Japan

* Correspondence: inada.ryozi.qr@tut.jp; Tel.: +81-532-446723

Abstract: Garnet-type Ta-doped $\text{Li}_7\text{La}_3\text{Zr}_2\text{O}_{12}$ (LLZO) ceramic solid electrolytes with Ga_2O_3 additive were synthesized using a conventional solid-state reaction process. When the amounts of Ga_2O_3 additive were below 2 mol %, the sintered sample has a dense structure composed of grains with an average size of 5 to 10 μm , whereas 3 mol % or more Ga_2O_3 addition causes a significant increase in grain size above several 10 to 100 μm , due to high-temperature sintering with a large amount of liquid Li-Ga-O phase. At room temperature, the highest total (bulk + grain-boundary) ionic conductivity of 1.1 mS cm^{-1} was obtained in the sample with 5 mol % Ga_2O_3 addition. However, this sample was shorted by Li dendrite growth into solid electrolyte at a current density below 0.2 mA cm^{-2} in galvanostatic testing of the symmetric cell with Li metal electrodes. The tolerance for Li dendrite growth is maximized in the sample sintered with 2 mol % Ga_2O_3 addition, which was shorted at 0.8 mA cm^{-2} in the symmetric cell. Since the interfacial resistance between Li metal and solid electrolyte was nearly identical among all samples, the difference in tolerance for Li dendrite growth is primarily attributed to the difference in microstructure of sintered samples depending on the amounts of Ga_2O_3 .



Citation: Yamazaki, Y.; Miyake, S.; Akimoto, K.; Inada, R. Effect of Ga_2O_3 Addition on the Properties of Garnet-Type Ta-Doped $\text{Li}_7\text{La}_3\text{Zr}_2\text{O}_{12}$ Solid Electrolyte. *Batteries* **2022**, *8*, 158. <https://doi.org/10.3390/batteries8100158>

Academic Editors: Catia Arbizzani and Carlos Zieber

Received: 12 July 2022

Accepted: 3 October 2022

Published: 6 October 2022

Publisher's Note: MDPI stays neutral with regard to jurisdictional claims in published maps and institutional affiliations.



Copyright: © 2022 by the authors. Licensee MDPI, Basel, Switzerland. This article is an open access article distributed under the terms and conditions of the Creative Commons Attribution (CC BY) license (<https://creativecommons.org/licenses/by/4.0/>).

Keywords: garnet; Li dendrite growth; solid electrolyte; solid state battery; Ga_2O_3 addition

1. Introduction

The application field of lithium (Li) ion batteries (LIBs) has expanded from a power source for portable electronic devices to a large-scale one for electric vehicles, plugin hybrid electric vehicles and stationary energy storage systems for load leveling. Along with the expansion of application fields for LIBs, not only further enhancement of the energy density of batteries but also higher safety and reliability are highly required.

Replacing a flammable organic liquid electrolyte with a non-flammable solid electrolyte is the most promising way to drastically improve battery safety. Inorganic ceramic Li ion conductors used as solid electrolytes are the key materials for achieving high performance all-solid-state batteries with high safety and reliability [1,2]. For solid-state battery applications, the materials used as solid electrolytes need good ionic conducting properties, plasticity and excellent chemical and electrochemical stabilities. Although oxide-based solid electrolyte materials have lower ionic conductivity and poorer deformability than sulfide-based ones, they have other advantages such as their chemical stability and ease of handling [3].

Among the various candidates, Li-stuffed garnet-type oxide with the composition of $\text{Li}_7\text{La}_3\text{Zr}_2\text{O}_{12}$ (LLZO) has been extensively investigated for application to solid-state batteries [4–10] because of the high ionic conductivity of 10^{-4} – $10^{-3} \text{ S cm}^{-1}$ at room temperature, good thermal stability, and moderate chemical stability in air. Although the dopant elements used to stabilize highly conductive cubic phase and improve ionic conducting properties may affect the electrochemical stability of LLZO against Li metal [11–13], LLZO generally exhibits good chemical and electrochemical stability against Li metal compared to other solid electrolyte materials.

The use of Li metal anodes with a large gravimetric theoretical capacity ($=3860 \text{ mAh g}^{-1}$) and the lowest electrode potential ($=-3.045 \text{ V}$ vs. standard hydrogen electrode) may result in a higher energy density of battery [14], while forming a solid–solid interface between LLZO and Li metal electrode remains a challenging issue. Poor interfacial connection due to the void formation at the cell assembling stage or by multiple charge and discharge cycling results in non-uniform Li plating. Intergranular Li dendrite growth occurs in polycrystalline LLZO when the cell is cycled at high current densities, resulting in internal short circuit failure [15–18].

The establishment of suppression technology for the possible Li dendrite growth into solid electrolyte has been a top priority for realizing solid-state Li-metal batteries. To date, significant research efforts have been made to reduce the interfacial charge-transfer resistance between LLZO and Li and improve the stability against Li plating/stripping at the interface. This includes eliminating secondary phases by polishing or chemical etching of the surface of LLZO [17,19–22], introducing thin film layers and thermal treatment at specific temperatures before and/or after contacting with Li [23–29], controlling the grain size and morphology of LLZO [30–38], and introducing three-dimensional porous LLZO structure at the interface to secure Li deposition sites and reduce effective current density [39,40]. Multiscale analysis for understanding the phenomenon occurring at the Li/LLZO interface and LLZO grain-boundary areas will play a critical role in overcoming this issue [41–48].

The microstructure of LLZO is one of the main factors for the stability of Li plating and stripping because the fracture toughness of polycrystalline LLZO is strongly influenced by density, grain size, and grain-boundary structure of LLZO [31,32,36–38]. In this research, we investigated the effect of Ga_2O_3 addition on the properties for Ta-doped LLZO ($\text{Li}_{6.55}\text{La}_3\text{Zr}_{1.55}\text{Ta}_{0.45}\text{O}_{12}$). It is expected that the added Ga_2O_3 reacts with Li in Ta-doped LLZO, and Li-Ga oxides are formed at the sintering process, including the liquid phase at $980\text{--}1000^\circ\text{C}$ [49]. The grain sizes, densities and electrochemical properties of sintered Ta-doped LLZO may be strongly influenced by the amounts of Ga_2O_3 added using liquid phase sintering with Li-Ga oxides. The optimal amounts of Ga_2O_3 are discussed in high ionic conductivity and tolerance for Li dendrite growth.

2. Materials and Methods

2.1. Synthesis and Characterization of Ta-Doped LLZO with Ga_2O_3 Addition

Calcined Ta-doped LLZO powder was synthesized using a conventional solid state reaction method. $\text{LiOH}\cdot\text{H}_2\text{O}$ (Kojundo Chemical Laboratory, Saitama, Japan, 99%), $\text{La}(\text{OH})_3$ (Kojundo chemical laboratory, 99.99%), ZrO_2 (Kojundo chemical laboratory, 98%) and Ta_2O_5 (Kojundo chemical laboratory, 99.9%) were weighed with the molar ratio of $\text{Li:La:Zr:Ta} = 7.205:3:1.55:0.45$ (adding 10% excess Li, considering the volatilization of Li during the sintering process). Here, the composition of Ta-doped LLZO was set to maximize the ionic conductivity based on our previous research [17,50]. Then, these starting materials were mixed and ground with ethanol for 5 h by planetary ball-milling (Planet M2-3F, Nagao System, Kawasaki, Japan) with zirconia balls with the diameter of 10 mm in a zirconia pot. The mixture was dried at 80°C and then calcined at 900°C for 6 h in the air using a Pt-5%Au alloy crucible.

Amounts of 1, 2, 3, 5 and 7 mol % Ga_2O_3 powder (Kojundo chemical laboratory, Saitama, Japan, 99.99%) was added to Ta-doped LLZO calcined powders and ground again by planetary ball-milling for 1 h. Then, the ball-milled powder was pelletized at 300 MPa by cold isostatic pressing. Finally, the pelletized samples were sintered at 1150°C for 15 h in air using a Pt-5%Au alloy crucible. The pellets were covered with the same mother powder to suppress Li loss and the formation of secondary phases by high sintering temperature. For comparison, samples without Ga_2O_3 addition were also prepared under the same condition.

The crystal phase for all sintered samples was evaluated by X-ray diffraction (XRD, RIGAKU Multiflex, Rigaku, Tokyo, Japan) using CuK α radiation ($\lambda = 0.15418$ nm), with a measurement range of $2\theta = 5\text{--}90^\circ$ and a step interval of 0.02° . The powder diffraction patterns were measured using a Bragg Brentano (focusing beam X-ray) optical system. Using X-ray diffraction (XRD) data, lattice constant for each sample was calculated by PDXL XRD analysis software (Rigaku, Tokyo, Japan). Microstructures for fractured cross-sectional surfaces of all sintered samples were observed using a scanning electron microscope (SEM, VE-8800, Keyence, Osaka Japan). The distributions of constituent elements in Ga₂O₃ added samples were investigated by energy dispersive X-ray analysis, using a field-emission SEM (FE-SEM, SU8000 Type II, Hitachi, Tokyo Japan). Brunauer–Emmett–Teller (BET) specific surface area for each sintered sample was obtained from N₂ adsorption/desorption isotherms recorded at 77 K, using a gas/vapor adsorption measurement apparatus (BELSORP MAX, Nippon Bel, Osaka Japan) in Aichi Center for Industry and Science Technology, Aichi, Japan.

2.2. Electrochemical Characterization of Ta-Doped LLZO with Ga₂O₃ Addition

Ionic conductivity for all sintered samples was evaluated using an impedance meter (IM3536, Hioki, Ueda, Japan) at temperatures ranging from 27 °C to 102 °C using an impedance meter (IM3536, Hioki) by electrochemical impedance spectroscopy (EIS) measurement with a frequency from 4 Hz to 2 MHz and applied voltage amplitude of 0.01 V. Before measuring conductivity, both parallel end surfaces of each sintered sample were polished and sputtered with Au films to serve as ion-blocking electrodes.

Then, all samples were used to evaluate the tolerance for Li dendrite growth through the galvanostatic cycling test using a symmetric cell with Li metal electrodes. Before assembling a symmetric cell, both end surfaces of the Ta-doped LLZO pellet were polished to remove surface contamination, and the pellet thickness was controlled to 0.16 cm. Both the end surfaces of the pellet were coated again with Au films (thickness = 100 nm) by sputtering. The pellet was then sandwiched with two Li metal foils with a diameter of 0.8 cm and thickness of 0.15 cm in an argon-filled glove box with a cell fixture (KP-Solid Cell, Hosen, Osaka, Japan), followed by heating at 175 °C for 5 h, to reduce the interfacial charge-transfer resistance (R_{int}) between Ta-doped LLZO and Li via an alloying reaction of Li and Au [23,25,27,34,49]. It is noted that the stacking pressure of each symmetric cell was set to 4 MPa. Both introduced Au interlayer and unifying the cell stacking pressures are effective in minimizing the difference in R_{int} among the samples as much as possible [35,50].

Each symmetric cell was cycled by changing the current densities from 0.05 to 1.0 mA cm⁻² and the cell voltage response was measured using a Battery Test System (TOSCAT-3100, TOYO SYSTEM, Iwaki, Japan) at 25 °C until the cell showed evidence of Li dendrite growth and propagation into a solid electrolyte. EIS measurement was carried out at room temperature using an impedance meter to characterize the resistance of each symmetric cell before and after the cycling test.

3. Results and Discussion

3.1. Structural Analysis of Ta-Doped LLZO with Ga₂O₃ Addition

Figure 1a presents XRD patterns for sintered Ta-doped LLZO with or without Ga₂O₃ addition. The calculated diffraction pattern based on the reported structural parameter for cubic LLZO is also plotted in Figure 1a as the reference [51]. All the peaks for sintered samples are well indexed as a cubic garnet-type structure and no other secondary phases were observed. Compared with the calculated peak pattern for cubic LLZO, the peaks for sintered samples are shifted toward a higher angle 2θ , attributing to the smaller lattice size by the partial replacement of Zr⁴⁺ (72 pm) in LLZO with smaller Ta⁵⁺ (64 pm) [17,50]. In Figure 1b, calculated lattice constant for all samples is plotted against the amount of Ga₂O₃ addition. It is evident that the lattice constant for Ga₂O₃ added samples is slightly lower than the sample without Ga₂O₃ addition. This indicates that Ga³⁺ is incorporated to the lattice of Ta-doped LLZO [12]. Except for 2 mol % Ga₂O₃ added sample, the lattice constant

tends to decrease with increasing Ga_2O_3 content. This suggests the possibility that the more Ga_2O_3 , the greater the incorporation amount of Ga in the lattice of Ta-doped LLZO.

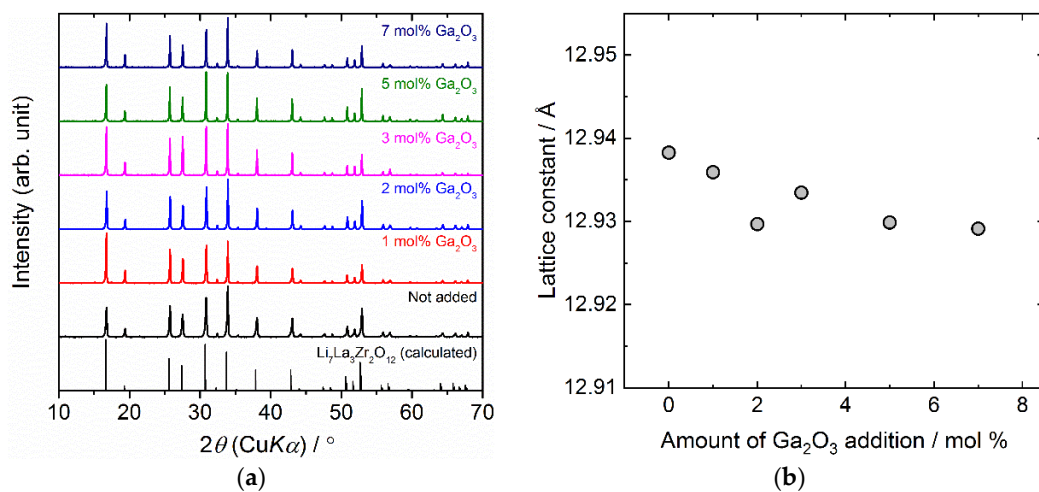


Figure 1. (a) X-ray diffraction patterns for sintered Ta-doped LLZO with or without Ga_2O_3 addition. (b) Calculated lattice constant for Ta-doped LLZO is plotted as a function of the amount of Ga_2O_3 addition. Enlarged data at $2\theta = 24\text{--}36^\circ$ and $24\text{--}56^\circ$ are shown in (b). Calculated pattern for LLZO is also plotted in (a) as the reference.

Figure 2 presents the SEM images for the fractured cross sections of sintered Ta-doped LLZO with or without Ga_2O_3 addition. Although the sintering conditions are identical among the samples, microstructures of sintered samples are strongly influenced by Ga_2O_3 addition. When the amounts of Ga_2O_3 additive were below 2 mol %, the sintered sample had a dense structure composed of grains with the averaged size of 5–10 μm , but a few abnormally grain growth areas were confirmed. Conversely, 3–7 mol % Ga_2O_3 addition causes a significant increase in grain size above several 10 μm and forms micrometer-sized pores. As reported in the literature [49], Ga_2O_3 forms a liquid Li-Ga-O phase at a temperature of 980–1000 $^\circ\text{C}$, which promotes the densification of LLZO and/or LLZO grain growth via liquid phase sintering. We believe that increasing the Li-Ga-O phase causes a significant increase in grain sizes, as observed with 3–7 mol % Ga_2O_3 added. Conversely, it is considered that micro-pores are formed by gas generation at the sintering process by the decomposition of Li_2CO_3 contained in calcined Ta-doped LLZO powder [52]. An increase in Ga_2O_3 addition greatly enhanced the sintering speed via liquid-phase sintering, but the release of gas from the Ta-doped LLZO pellet was inhibited by excess Ga_2O_3 addition.

Figure 3 depicts the distributions of constituent elements (O, La, Zr, Ta and Ga, excluding Li) on the fractured cross-sectional surfaces of Ta-doped LLZO sintered with 2 mol % and 5 mol % Ga_2O_3 addition. It is confirmed that the distribution of La, Zr and Ta seems to be very similar in the SEM observation area for each sample. Interestingly, Ga distributes on the surface of Ta-doped LLZO grains, suggesting that the small amount of Ga may be incorporated into Ta-doped LLZO. Furthermore, several segregation areas with Ga and O are confirmed mainly at the grain-boundary regions, which seems more remarkable in 5 mol % Ga_2O_3 added samples. Although the secondary phase by Ga_2O_3 addition was not detected in XRD measurements (Figure 1), Ga_2O_3 added sample contains a tiny amount of Ga-containing oxide.

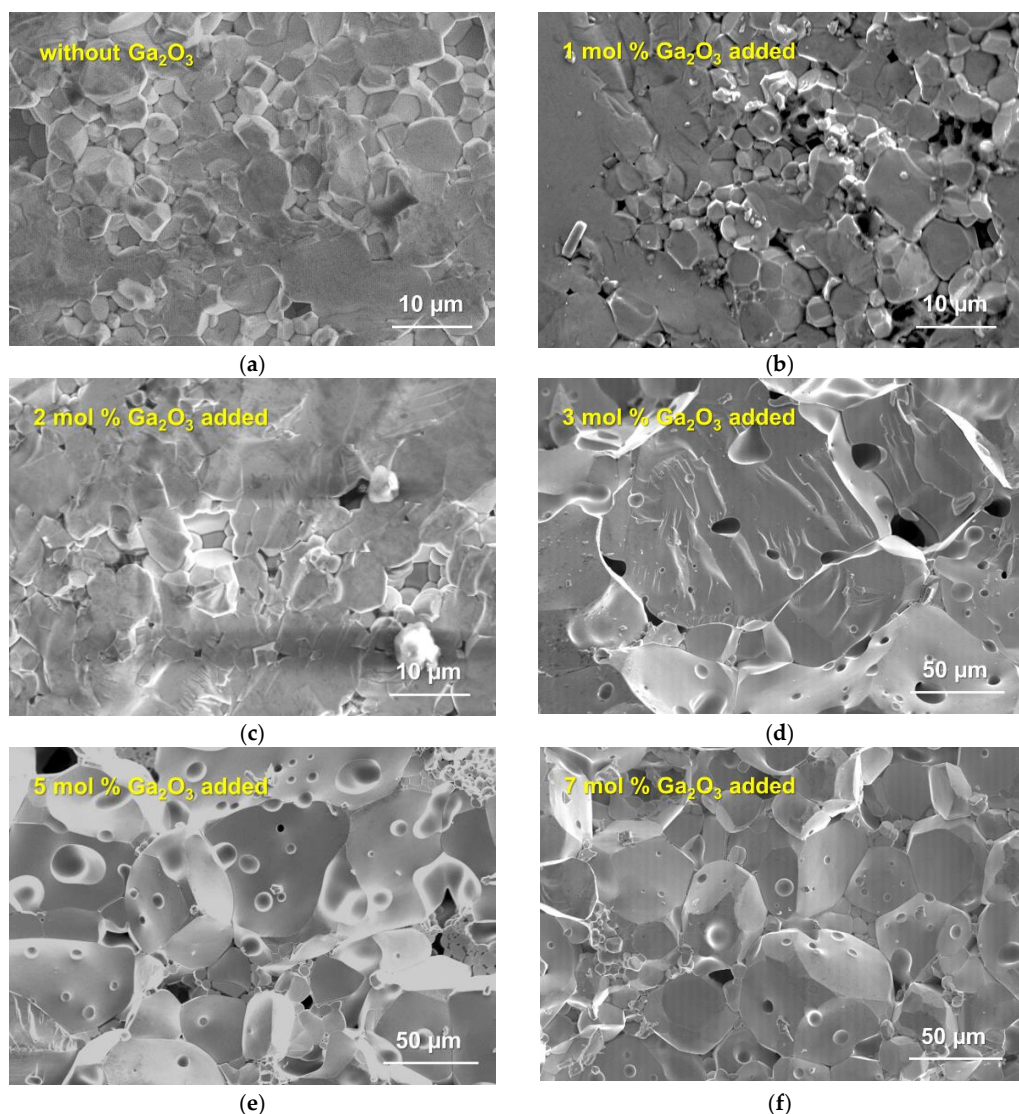


Figure 2. SEM images for fractured cross-sectional surfaces of sintered Ta-doped LLZO: (a) without Ga_2O_3 addition, (b) 1 mol % Ga_2O_3 addition, (c) 2 mol % Ga_2O_3 addition, (d) 3 mol % Ga_2O_3 addition, (e) 5 mol % Ga_2O_3 addition and (f) 7 mol % Ga_2O_3 addition. Note that the scale bars in (a–c) are different from (d–f).

Table 1 shows the BET specific surface area A_{surf} and density ρ for Ta-doped LLZO sintered with and without Ga_2O_3 addition. A_{surf} for each sample was obtained from N_2 adsorption/desorption isotherms (Figure S1 in Supplementary Materials). The density ρ of each sample is calculated using mass and geometrical parameters of each sample. It is considered that A_{surf} is affected by both the particle size and density of each sample. Compared to sample without Ga_2O_3 addition, 1 and 2 mol % Ga_2O_3 added samples have higher density and smaller A_{surf} . Since the grain growth in these two samples is not so remarkable (Figure 2b,c), A_{surf} becomes smaller than that for sample without Ga_2O_3 addition. On the other hand, 3–7 mol % Ga_2O_3 added samples have slightly lower density than sample without Ga_2O_3 addition, but the grain size for these three samples is very large. Therefore, it is considered that A_{surf} for 3–7 mol % Ga_2O_3 added samples becomes smaller than that for sample without Ga_2O_3 addition.

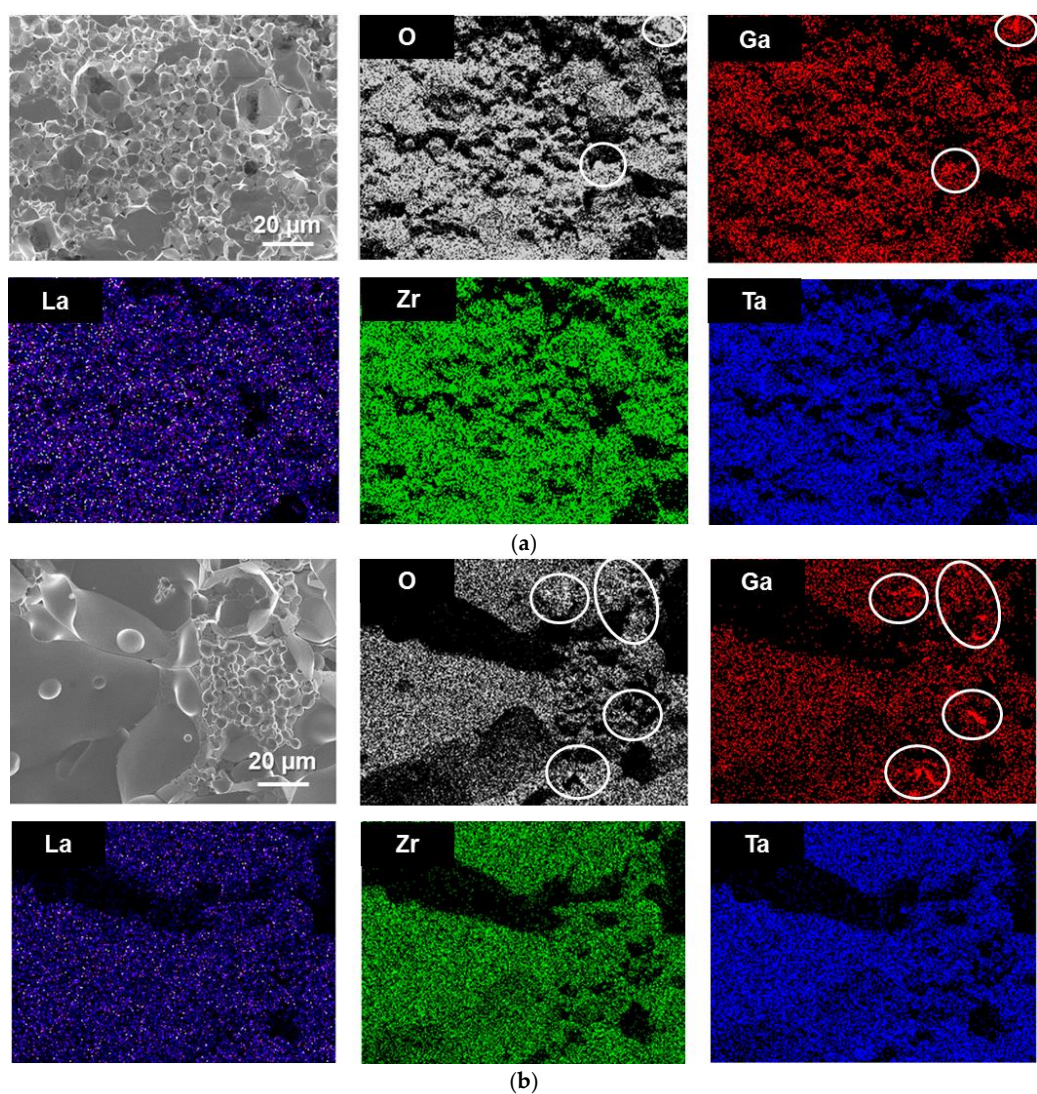


Figure 3. Constituent element (La, Zr, Ta, Ga and O) distributions on the fractured cross-sectional surfaces of Ta-doped LLZO sintered with (a) 2 mol % Ga₂O₃ and (b) 5 mol % Ga₂O₃. The segregation areas of Ga and O in each sample are marked with white-lined circles.

Table 1. Densities ρ and BET specific surface areas A_{surf} of Ta-doped LLZO sintered with or without Ga₂O₃ addition.

Ga ₂ O ₃ Addition/mol %	$\rho/\text{g cm}^{-3}$	$A_{\text{surf}}/\text{m}^2 \text{ g}^{-1}$
Not added	4.84	2.418
1	4.96	1.488
2	4.98	1.139
3	4.76	1.475
5	4.81	1.163
7	4.76	1.144

3.2. Ionic Conductin Properties of Ta-Doped LLZO with Ga₂O₃ Addition

Figure 4 presents the Nyquist plots for complex impedance $Z' + jZ''$ of all sintered samples with Au blocking electrodes measured at room temperature. Real and imaginary parts of complex impedance Z' and Z'' multiplied by a factor of S/t are plotted for direct comparison of the data, where S and t are the surface area and thickness of each sample. At room temperature, the plot for all samples consists of a linear tail below 0.1 MHz and a small

part of the semicircle above 0.1 MHz. The intersection point of the exterior straight line of the data in the linear tail and the Z' axis nearly corresponds to the total (bulk + grain-boundary) resistance R_{total} of each sample. The R_{total} values for Ga_2O_3 added samples are confirmed to be slightly smaller than the sample without Ga_2O_3 addition, suggesting that Ga_2O_3 addition has a positive effect on ionic conduction in sintered Ta-LLZO. Only for the samples sintered with 1 and 2 mol % Ga_2O_3 addition, the portion of semicircle for grain-boundary resistance is observed (Figure 4a), but its contribution in total resistance is minimal.

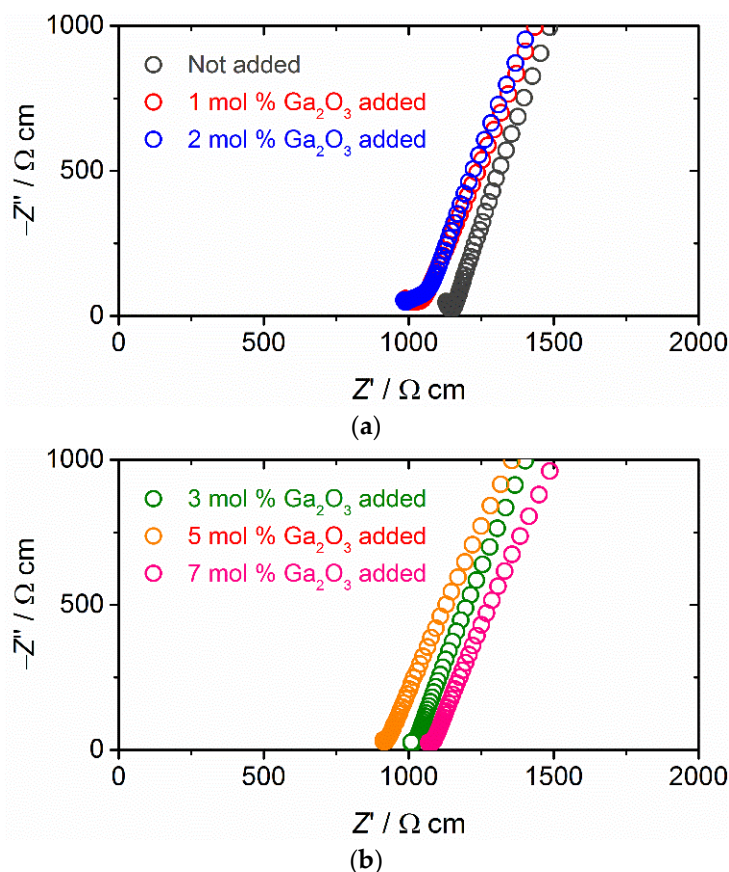


Figure 4. Nyquist plots for complex impedance $Z' + jZ''$ in Ta-doped LLZO sintered with or without Ga_2O_3 addition measured at 27 $^{\circ}\text{C}$: (a) 0, 1 and 2 mol % Ga_2O_3 addition and (b) 3, 5 and 7 mol % Ga_2O_3 addition. Au ionic blocking electrodes were used for the measurement.

Figure 5 presents the density ρ and total ionic conductivity σ_{total} at room temperature for sintered Ta-doped LLZO plotted against the amounts of Ga_2O_3 addition. As can be seen, the Ga_2O_3 amount dependence of σ_{total} is slightly different. Slightly higher densities of 1 and 2 mol % Ga_2O_3 added samples than the sample without Ga_2O_3 addition could be due to the small gaps at the grain-boundaries being filled with Ga-containing oxides, but this is difficult to confirm in Figures 2a–c and 3a. In contrast, a slight decrease in densities of samples sintered with 3–7 mol % Ga_2O_3 addition may be attributed to the formation of micrometer-sized pores, as shown in Figure 2d–f.

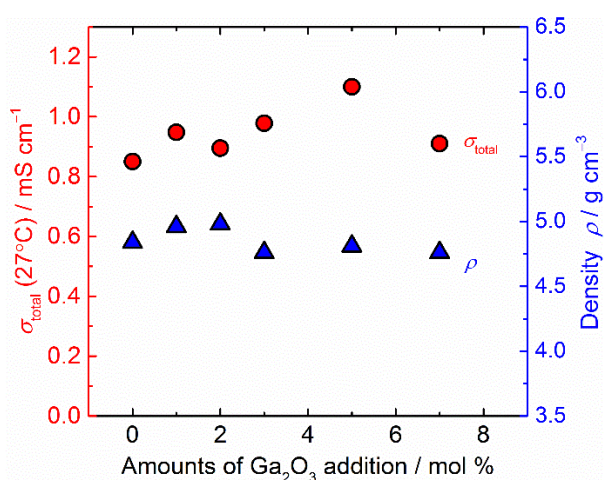


Figure 5. Density ρ and total ionic conductivity σ_{total} at room temperature of all sintered samples are plotted against the amounts of Ga_2O_3 addition.

For the sample with 5 mol % Ga_2O_3 addition, σ_{total} shows the maximum value ($\sim 1.1 \text{ mS cm}^{-1}$), and other Ga_2O_3 added samples have a slightly higher σ_{total} than those without Ga_2O_3 addition. Since the contribution of grain-boundary resistance is very small for all samples (Figure 4), the change in σ_{total} is mainly governed by the difference in bulk conductivity. Small amounts of Ga inclusion in cubic garnet structure may influence the Li distribution in the crystal lattice and bulk ionic conductivity [12,53]. The effect of simultaneous doping of Ta and Ga on the structure and bulk ionic conductivity of LLZO should be investigated in the future. From the temperature dependence of σ_{total} (Figure S2 in Supplementary Materials), the activation energy E_a for ionic conduction in each sample was estimated and summarized in Table 1 together with σ_{total} and ρ . At room temperature, σ_{total} increases slightly and E_a tends to become lower by Ga_2O_3 addition.

3.3. Tolerance for Li Dendrite Growth of Ta-Doped LLZO with Ga_2O_3 Addition

Next, we discussed the tolerance for Li dendrite growth in Ta-doped LLZO sintered with or without Ga_2O_3 addition. Nyquist plots for complex impedance $Z' + jZ''$ at room temperature for Li symmetric cells composed of each solid electrolyte sample are shown in Figure 6. Before the galvanostatic testing, the plot for each symmetric cell is composed of a large semicircle with a characteristic frequency from 2.5 to 5 MHz and a small distorted one at frequency range from 100 Hz to 0.1 MHz. The contribution of ionic conduction for sintered Ta-LLZO with or without Ga_2O_3 addition was obtained using high frequency ($>0.1 \text{ MHz}$) impedance data, and the diameters of the semicircle at higher frequencies well correlate with the difference in σ_{total} , as summarized in Table 2.

Table 2. Total ionic conductivity σ_{total} at room temperature and activation energy E_a for Ta-doped LLZO sintered with or without Ga_2O_3 addition.

Ga_2O_3 Addition/mol %	σ_{total} at 27°C /mS cm $^{-1}$	E_a /eV
Not added	0.85	0.38
1	0.95	0.31
2	0.90	0.36
3	0.98	0.31
5	1.1	0.33
7	0.91	0.30

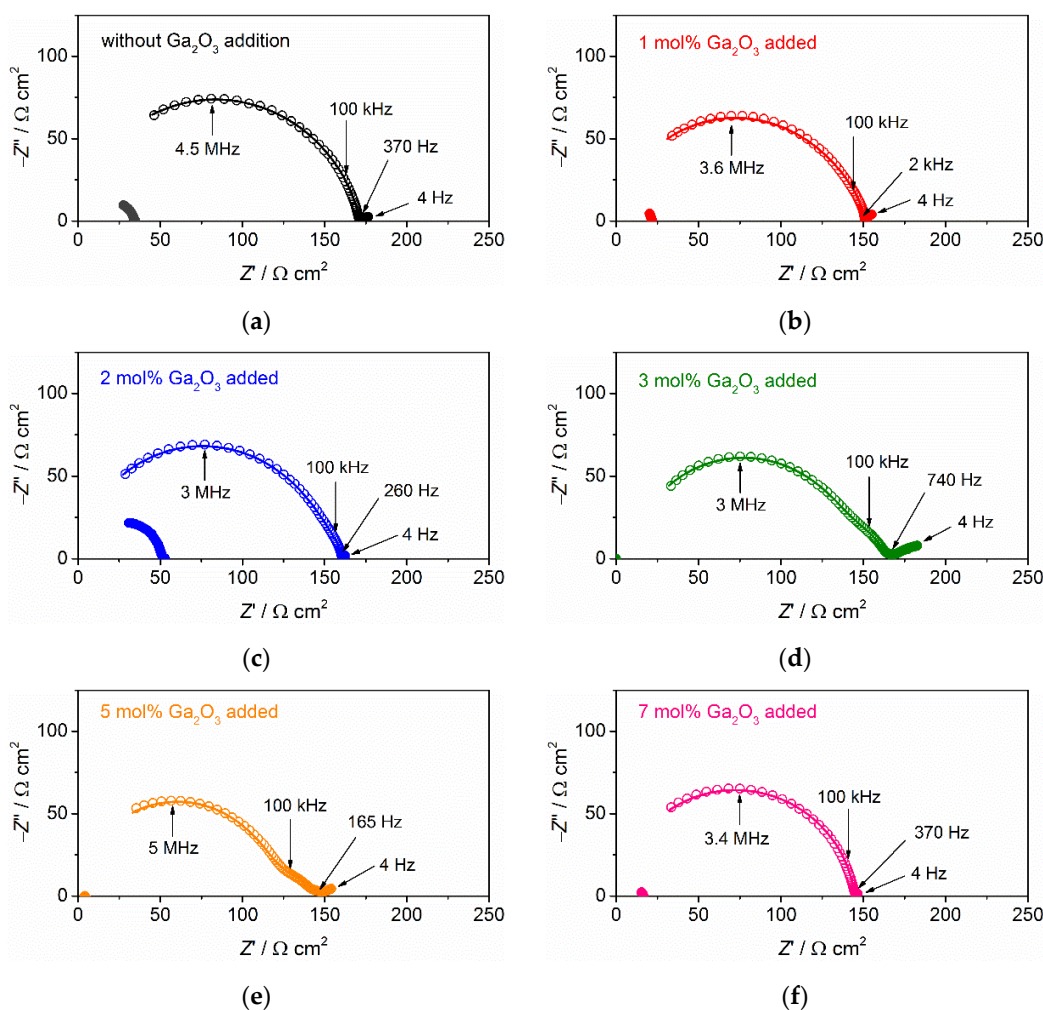


Figure 6. Nyquist plots for complex impedance $Z' + jZ''$ at 27 °C in symmetric cells composed of Li metal electrodes and Ta-doped LLZO: (a) without Ga_2O_3 addition, (b) 1 mol % Ga_2O_3 addition, (c) 2 mol % Ga_2O_3 addition, (d) 3 mol % Ga_2O_3 addition, (e) 5 mol % Ga_2O_3 addition and (f) 7 mol % Ga_2O_3 addition. Blank and solid symbols correspond to the impedance data before and after the galvanostatic cycling test, respectively. The solid lines are the fitting curves for the data before galvanostatic testing by the equivalent circuit.

The contribution of interfacial charge transfer resistance R_{int} is limited to frequencies ranging from 100 Hz to 0.1 MHz [16,49]. For the cells with 3 mol % and 5 mol % added Ta-doped LLZO, the contribution of R_{int} is confirmed in the plot, while for other cells, it is considered that the contribution of R_{int} is partly contained in a large semicircle. The electrochemical impedance of each symmetric cell is fitted by the equivalent circuit model composed of $(R_{\text{SE}} - Q_{\text{SE}})(R_{\text{int}} - Q_{\text{int}})(R_{\text{pore}} - Q_{\text{pore}})$ (Figure S3 in Supplementary Materials) [54], where R_{SE} and Q_{SE} are the resistance and constant phase angle element of a solid electrolyte, Q_{int} is the constant phase angle element at the interface between solid electrolyte and Li metal, R_{pore} and Q_{pore} are the contributions from pores at the interface. Figure 6 depicts the fitting curves for all samples and experimental data. Table 3 summarizes R_{int} and Q_{int} for all samples. Estimated R_{int} values vary in the range of 2–20 $\Omega \text{ cm}^2$ and Q_{int} values lie in the range from 10^{-7} to 10^{-6} F. The difference in R_{int} among the tested cells could be attributed to variations in the surface microstructures of the samples before the attachment of Li metals.

Table 3. R_{int} and Q_{int} are obtained by equivalent circuit fitting electrochemical impedance of symmetric cells composed of Ta-doped LLZO with or without Ga_2O_3 addition.

Ga ₂ O ₃ Addition/mol %	$R_{int}/\Omega \text{ cm}^2$	Q_{int}/F
Not added	9.5	1.1×10^{-7}
1	6.0	5.8×10^{-7}
2	6.7	2.3×10^{-7}
3	10.1	1.2×10^{-7}
5	17.5	2.3×10^{-6}
7	2.0	4.7×10^{-7}

Figure 7 shows the voltage response in galvanostatic cycling of each symmetric cell tested at room temperature. Here, the applied current density was firstly set to 0.05 mA cm^{-2} and was increased to 0.05 mA cm^{-2} around five cycles. As can be seen, cell voltage increases gradually with applied current density for each cell, but the sudden drop and fluctuation of cell voltage occur when the current density reaches a specific value. This indicates potential Li dendrite growth and propagation into a solid electrolyte. We confirmed the decrease in cell impedance shown in Figure 6, after the cycling test of each cell, as discussed later. Several symmetric cells have large residual impedances, and the plots are shaped like part of a semicircle, suggesting that they are not shorted completely [50].

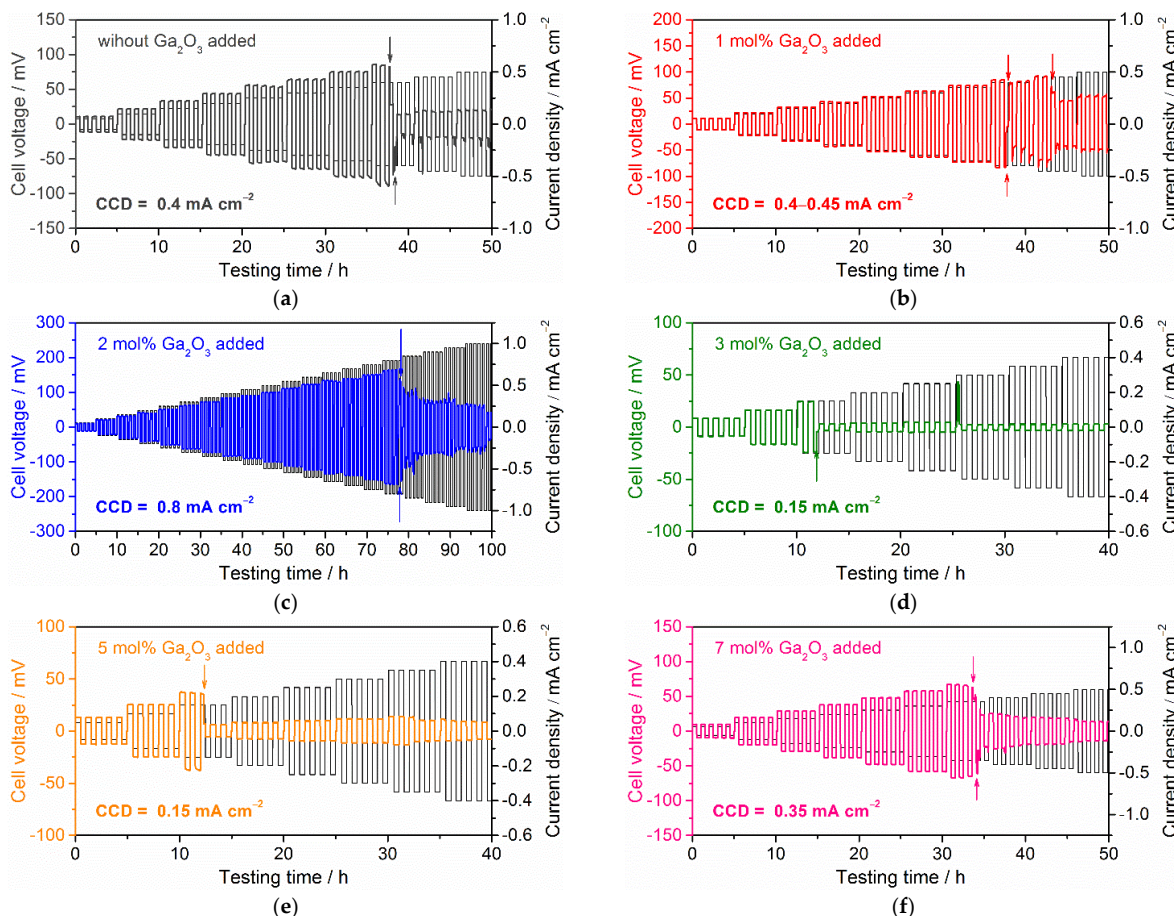


Figure 7. Cell voltage changes during galvanostatic cycling test at 25°C for Li symmetric cell with Ta-doped LLZO: (a) without Ga_2O_3 addition, (b) 1 mol % Ga_2O_3 addition, (c) 2 mol % Ga_2O_3 addition, (d) 3 mol % Ga_2O_3 addition, (e) 5 mol % Ga_2O_3 addition and (f) 7 mol % Ga_2O_3 addition. The arrows in each graph represent the sudden voltage drops caused by possible Li dendrite growth into a solid electrolyte.

The current density at which Li dendrite growth and propagation into a solid electrolyte occurred is commonly called the critical current density (CCD). CCD may be affected by the testing method because the interface condition between Li metal and a solid electrolyte is generally changed by the area-specific capacity and cycling numbers of Li plating/stripping [7,19–21]. In order to directly compare the CCD values reported by other groups, the test conditions must be considered as well. In this study, the method and condition for the galvanostatic cycling test are unified, and the difference in R_{int} between the samples is adjusted to be as small as we can. Consequently, CCD obtained in this work can be used for discussing the difference in the tolerance for Li dendrite growth depending on the microstructure of the solid electrolyte. CCD for 1 mol % Ga_2O_3 added sample (Figure 7b) is 0.40–0.45 mA cm^{-2} and close to the sample without Ga_2O_3 addition (Figure 7a). A total of 2 mol % Ga_2O_3 added sample shows the highest CCD of 0.8 mA cm^{-2} , while 3 mol % or more Ga_2O_3 added samples show CCD below 0.4 mA cm^{-2} . CCD of 3 and 5 mol % Ga_2O_3 added samples are the lowest ($=0.15 \text{ mA cm}^{-2}$) while 7 mol % Ga_2O_3 added sample shows higher CCD of 0.35 mA cm^{-2} . The difference in R_{int} among 3–7 mol % Ga_2O_3 added samples may cause the difference in CCD, as confirmed in Figure 6. A larger R_{int} in 3 and 5 mol % Ga_2O_3 added samples may result in lower CCD.

In Figure 8, σ_{total} and CCD are plotted against the amounts of Ga_2O_3 addition. The optimum amount of Ga_2O_3 added to Ta-doped LLZO for σ_{total} and CCD is completely different. Although the conductivity shows the highest in 5 mol % Ga_2O_3 added sample, the difference in conductivity between samples is small. In contrast to the difference in conductivity, the microstructure of the solid electrolyte and the quality of the interfacial bonding strongly influence stability for Li plating and stripping and tolerance for Li dendrite. Notably, using 2 mol % Ga_2O_3 added sample, we fabricated another Li symmetric cell with larger R_{int} ($>50 \Omega \text{ cm}^2$) by changing the cell stacking condition. A galvanostatic cycling test was performed under the same condition. Although the polarization becomes larger by large R_{int} , the cell was cycled at a current density above 0.5 mA cm^{-2} without any evidence of a short circuit by Li dendrite growth. CCD attained 0.6 mA cm^{-2} (Figures S4 and S5 in Supplementary Materials), which is better than the symmetric cells with other solid electrolyte samples and lower R_{int} shown in Figure 7. This result supports the present work that the optimum Ga_2O_3 amount added to Ta-doped LLZO is 2 mol % to obtain higher CCD. Excessive addition of Ga_2O_3 causes deterioration of the tolerance for Li dendrite growth of Ta-doped LLZO due to the abnormal grain growth promoted by liquid-phase sintering.

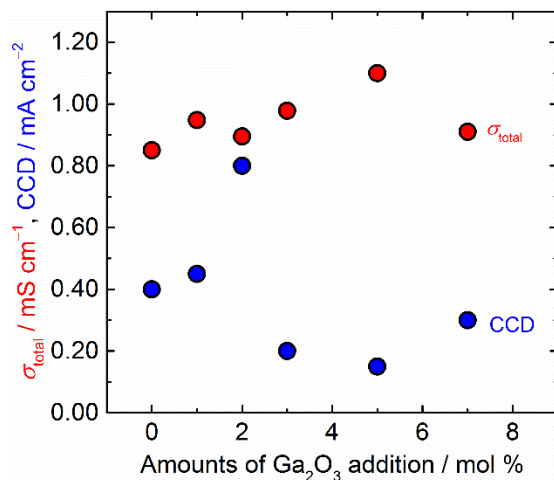


Figure 8. Total ionic conductivity σ_{total} and critical current density (CCD) at room temperature of all sintered samples are plotted against the amounts of Ga_2O_3 addition.

Although the present results reported here is the opposite of the result obtained in hot-pressed Al-doped LLZO followed by high temperature (1300 °C) and long-time

annealing in an Ar atmosphere [35], we believe dense structure with tightly connected small Ta-doped LLZO grains (below 10 μm) is suitable for higher CCD because uniform and a dense structure composed of small-sized LLZO grains effectively enhance the fracture toughness of sintered sample [36–38]. Furthermore, grain-boundary composed of large-sized LLZO grains tends to behave like a path through which Li dendrite can easily propagate [30,32]. Thus, we are carefully optimizing the sintering temperature and time for 2 mol % Ga_2O_3 added Ta-doped LLZO to reduce the grain size and improve structural uniformity to enhance the tolerance for Li dendrite growth and the results will be presented in a forthcoming paper.

4. Conclusions

We synthesized Ga_2O_3 added Ta-doped LLZO with garnet-type structure using a conventional solid-state reaction method and examined their microstructures and electrochemical properties. When the amounts of Ga_2O_3 additive were below 2 mol %, the sintered sample has a dense structure mainly composed of grains with the averaged size of 5–10 μm , whereas 3 mol % or more Ga_2O_3 addition causes the significant increase in grain size above several 10 to 100 μm , due to the liquid-phase sintering with a large amount of Li-Ga-O. The highest total ionic conductivity of 1.1 mS cm^{-1} at room temperature was observed in a 5 mol % Ga_2O_3 added sample, but in galvanostatic testing of the symmetric cell with Li metal electrodes, this sample was shorted by Li dendrite growth into solid electrolyte below 0.2 mA cm^{-2} . The tolerance for Li dendrite growth is maximized in the sample sintered with 2 mol % Ga_2O_3 addition, which was shorted at 0.8 mA cm^{-2} in the symmetric cell. Since the method and condition for the galvanostatic cycling test are unified and the difference in R_{int} between the samples is adjusted to be as small as possible, the difference in CCD among the samples with different amounts of Ga_2O_3 addition is mainly governed by the difference in microstructures. A dense structure with tightly connected small Ta-doped LLZO grains is suitable to improve the tolerance for Li dendrite growth.

Supplementary Materials: The following are available online at <https://www.mdpi.com/article/10.3390/batteries8100158/s1>, Figure S1: N_2 gas adsorption/desorption isotherms for Ta-doped LLZO with or without Ga_2O_3 addition, Figure S2: Temperature dependence for total ionic conductivity σ_{total} for Ta-doped LLZO sintered with or without Ga_2O_3 addition, Figure S3: Equivalent circuit for fitting the electrochemical impedance of Li symmetric cell, Figure S4: Nyquist plot for complex impedance and voltage response in galvanostatic cycling test for Li symmetric cell with larger interfacial resistance R_{int} composed of 2 mol % Ga_2O_3 added Ta-doped LLZO, Figure S5: Change in cell resistance R_{cell} during galvanostatic cycling test for Li symmetric cells with different R_{int} composed of 2 mol % Ga_2O_3 added Ta-doped LLZO.

Author Contributions: Conceptualization, Y.Y. and R.I.; methodology, Y.Y., S.M., K.A. and R.I.; validation, Y.Y., S.M., K.A. and R.I.; formal analysis, Y.Y., S.M., K.A. and R.I.; investigation, Y.Y., S.M., K.A. and R.I.; resources, R.I.; data curation, Y.Y., S.M., K.A. and R.I.; writing—original draft preparation, Y.Y. and R.I.; writing—review and editing, R.I.; supervision, R.I.; project administration, R.I.; funding acquisition, R.I. All authors have read and agreed to the published version of the manuscript.

Funding: This work was partly supported by Grant-in-Aid for Scientific Research (JSPS KAKENHI) Grant Number 19H02128 and 22H01468 from the Japan Society for the promotion of Science (JSPS).

Data Availability Statement: The data presented in this study are available on request from the corresponding author.

Acknowledgments: We acknowledged the support of the Cooperative Research Facility Center at Toyohashi University of Technology. We would like to thank Yoshitada Abe in Aichi Center for Industry and Science Technology for his cooperation in BET specific surface area measurement of our samples.

Conflicts of Interest: The authors declare no conflict of interest. The funders had no role in the design of the study; in the collection, analyses, or interpretation of data; in the writing of the manuscript, or in the decision to publish the results.

References

1. Zheng, F.; Kotobuki, M.; Song, S.; Lei, M.O.; Lu, L. Review on solid electrolytes for all-solid-state lithium-ion batteries. *J. Power Sources* **2018**, *389*, 198–213. [[CrossRef](#)]
2. Takada, K. Progress in solid electrolytes toward realizing solid-state lithium batteries. *J. Power Sources* **2018**, *394*, 74–85. [[CrossRef](#)]
3. Ren, Y.; Chen, K.; Chen, R.; Liu, T.; Zhang, Y.; Nan, C. Oxide electrolytes for lithium batteries. *J. Am. Ceram. Soc.* **2015**, *98*, 3603–3623. [[CrossRef](#)]
4. Murugan, R.; Thangadurai, V.; Weppner, W. Fast lithium ion conduction in garnet-type $\text{Li}_7\text{La}_3\text{Zr}_2\text{O}_{12}$. *Angew. Chem. Int. Ed.* **2007**, *46*, 7778–7781. [[CrossRef](#)]
5. Samson, A.J.; Hofstetter, K.; Bag, S.; Thangadurai, V. A bird’s-eye view of Li-stuffed garnet-type $\text{Li}_7\text{La}_3\text{Zr}_2\text{O}_{12}$ ceramic electrolytes for advanced all-solid-state Li batteries. *Energy Environ. Sci.* **2019**, *12*, 2957–2975. [[CrossRef](#)]
6. Wang, C.; Fu, K.; Palakkathodi, K.S.; McOwen, D.W.; Zhang, L.; Hitz, G.T.; Nolan, A.; Samson, A.; Wachsman, E.D.; Mo, Y.; et al. Garnet-type solid-state electrolytes: Materials, interfaces, and batteries. *Chem. Rev.* **2020**, *120*, 4257–4300. [[CrossRef](#)]
7. Alexander, G.V.; Indu, M.S.; Murugan, R. Review on the critical issues for the realization of all-solid-state lithium metal batteries with garnet electrolyte: Interfacial chemistry, dendrite growth, and critical current densities. *Lionics* **2021**, *27*, 4105–4126. [[CrossRef](#)]
8. Patra, S.; Narayanasamy, J.; Panneerselvam, M.R. Review—Microstructural modification in lithium garnet solid-state electrolytes: Emerging trends. *J. Electrochem. Soc.* **2022**, *169*, 030548. [[CrossRef](#)]
9. Chen, B.; Sarkar, S.; Kammampata, S.P.; Zhou, C.; Thangadurai, V. Li-stuffed garnet electrolytes: Structure, ionic conductivity, chemical stability, interface, and applications. *Can. J. Chem.* **2022**, *100*, 311–319. [[CrossRef](#)]
10. Kim, Y.; Yoo, A.; Schmidt, R.; Sharafi, A.; Lee, H.; Wolfenstine, J.; Sakamoto, J. Electrochemical Stability of $\text{Li}_{6.5}\text{La}_3\text{Zr}_{1.5}\text{M}_{0.5}\text{O}_{12}$ ($\text{M} = \text{Nb}$ or Ta) against Metallic Lithium. *Front. Energy Res.* **2016**, *4*, 20. [[CrossRef](#)]
11. Zhu, Y.; Connell, J.G.; Tepavcevic, S.; Zapol, P.; Garcia-Mendez, R.; Taylor, N.J.; Sakamoto, J.; Ingram, B.J.; Curtiss, L.A.; Freeland, J.W.; et al. Dopant-dependent stability of garnet solid electrolyte interfaces with lithium metal. *Adv. Energ. Mater.* **2019**, *9*, 1803440. [[CrossRef](#)]
12. Tsai, C.-L.; Tran, N.T.T.; Schierholz, R.; Liu, Z.; Windmüller, A.; Lin, C.-A.; Zu, Q.; Lu, X.; Yu, S.; Tempel, H.; et al. Instability of Ga-substituted $\text{Li}_7\text{La}_3\text{Zr}_2\text{O}_{12}$ toward metallic Li. *J. Mater. Chem. A* **2022**, *10*, 10998–11009. [[CrossRef](#)]
13. McClelland, I.; El-Shinawi, H.; Booth, S.G.; Regoutz, A.; Clough, J.; Altus, S.; Cussen, E.J.; Baker, P.J.; Cussen, S.A. The role of the reducible dopant in solid electrolyte–lithium metal interfaces. *Chem. Mater.* **2022**, *34*, 5054–5064. [[CrossRef](#)]
14. Wang, M.; Carmona, E.; Gupta, A.; Albertus, P.; Sakamoto, J. Enabling “lithium-free” manufacturing of pure lithium metal solid-state batteries through in situ plating. *Nat. Commun.* **2020**, *11*, 5201. [[CrossRef](#)] [[PubMed](#)]
15. Ren, Y.; Shen, Y.; Lin, Y.; Nan, C.-W. Direct observation of lithium dendrites inside garnet-type lithium-ion solid electrolyte. *Electrochim. Commun.* **2015**, *57*, 27–30. [[CrossRef](#)]
16. Cheng, E.J.; Sharafi, A.; Sakamoto, J. Intergranular Li metal propagation through polycrystalline $\text{Li}_{6.25}\text{Al}_{0.25}\text{La}_3\text{Zr}_2\text{O}_{12}$ ceramic electrolyte. *Electrochim. Acta* **2017**, *223*, 85–91. [[CrossRef](#)]
17. Inada, R.; Yasuda, S.; Hosokawa, H.; Saito, M.; Tojo, T.; Sakurai, Y. Formation and stability of interface between garnet-type Ta-doped $\text{Li}_7\text{La}_3\text{Zr}_2\text{O}_{12}$ solid electrolyte and lithium metal electrode. *Batteries* **2018**, *4*, 26. [[CrossRef](#)]
18. Kazyak, E.; Garcia-Mendez, R.; LePage, W.S.; Sharafi, A.; Davis, A.L.; Sanchez, A.J.; Chen, K.-H.; Haslam, C.; Sakamoto, J.; Dasgupta, N.P. Li penetration in ceramic solid electrolytes: Operando microscopy analysis of morphology, propagation, and reversibility. *Matter* **2020**, *2*, 1025–1048. [[CrossRef](#)]
19. Sharafi, A.; Kazyak, E.; Davis, A.L.; Yu, S.; Thompson, T.; Siegel, D.J.; Dasgupta, N.P.; Sakamoto, J. Surface chemistry mechanism of ultra-low interfacial resistance in the solid-state electrolyte $\text{Li}_7\text{La}_3\text{Zr}_2\text{O}_{12}$. *Chem. Mater.* **2017**, *29*, 7961–7968. [[CrossRef](#)]
20. Basappa, R.H.; Ito, T.; Yamada, H. Contact between garnet-type solid electrolyte and lithium metal anode: Influence on charge transfer resistance and short circuit prevention. *J. Electrochem. Soc.* **2017**, *164*, A666–A671. [[CrossRef](#)]
21. Taylor, N.J.; Stangeland-Molo, S.; Haslam, C.G.; Sharafi, A.; Thompson, T.; Wang, M.; Garcia-Mendez, R.; Sakamoto, J. Demonstration of high current densities and extended cycling in the garnet $\text{Li}_7\text{La}_3\text{Zr}_2\text{O}_{12}$ solid electrolyte. *J. Power Sources* **2018**, *396*, 314–318. [[CrossRef](#)]
22. Motoyama, M.; Tanaka, Y.; Yamamoto, T.; Tsuchimine, N.; Kobayashi, S.; Iriyama, Y. The Active interface of Ta-doped $\text{Li}_7\text{La}_3\text{Zr}_2\text{O}_{12}$ for Li plating/stripping revealed by acid aqueous etching. *ACS Appl. Energy Mater.* **2019**, *2*, 6720–6731. [[CrossRef](#)]
23. Tsai, C.-L.; Roddatis, V.; Chandran, C.V.; Ma, Q.; Uhlenbruck, S.; Bram, M.; Heitjans, P.; Guillon, O. $\text{Li}_7\text{La}_3\text{Zr}_2\text{O}_{12}$ interface modification for Li dendrite prevention. *ACS Appl. Mater. Interfaces* **2016**, *8*, 10617–10626. [[CrossRef](#)]
24. Han, X.; Gong, Y.; Fu, K.; He, X.; Hitz, G.T.; Dai, J.; Pearse, A.; Liu, B.; Wang, H.; Rublo, G.; et al. Negating interfacial impedance in garnet-based solid-state Li metal batteries. *Nat. Mater.* **2017**, *16*, 572–579. [[CrossRef](#)] [[PubMed](#)]
25. Huang, X.; Lu, Y.; Guo, H.; Song, Z.; Xiu, T.; Badding, M.E.; Wen, Z. None-mother-powder method to prepare dense Li-garnet solid electrolytes with high critical current density. *ACS Appl. Energy Mater.* **2018**, *1*, 5355–5365. [[CrossRef](#)]
26. Zhou, C.; Samson, A.J.; Hofstetter, K.; Thangadurai, V. A surfactant-assisted strategy to tailor Li-ion charge transfer interfacial resistance for scalable all-solid-state Li batteries. *Sustain. Energy Fuels* **2018**, *2*, 2165–2170. [[CrossRef](#)]
27. Sastre, J.; Futscher, M.H.; Pompizi, L.; Aribia, A.; Priebe, A.; Overbeck, J.; Stiefel, M.; Tiwari, A.N.; Romanyuk, Y.E. Blocking lithium dendrite growth in solid-state batteries with an ultrathin amorphous Li-La-Zr-O solid electrolyte. *Commun. Mater.* **2021**, *2*, 76. [[CrossRef](#)]

28. Du, M.; Sun, Y.; Liu, B.; Chen, B.; Liao, K.; Ran, R.; Cai, R.; Zhou, W.; Shao, Z. Smart construction of an intimate lithium | garnet interface for all-solid-state batteries by tuning the tension of molten lithium. *Adv. Funct. Mater.* **2021**, *31*, 2101556. [CrossRef]
29. Guo, S.; Wu, T.-T.; Sun, G.; Zhang, S.-D.; Li, B.; Zhang, H.-S.; Qi, M.-Y.; Liu, X.-H.; Cao, A.-M.; Wan, L.-J. Interface engineering of a ceramic electrolyte by Ta_2O_5 nanofilms for ultrastable lithium metal batteries. *Adv. Funct. Mater.* **2022**, *32*, 2201498. [CrossRef]
30. Cheng, L.; Chen, W.; Kunz, M.; Persson, K.; Tamura, N.; Chen, G.; Doeff, M. Effect of surface microstructure on electrochemical performance of garnet solid electrolytes. *ACS Appl. Mater. Interfaces* **2015**, *7*, 2073–2081. [CrossRef]
31. Sharafi, A.; Meyer, H.M.; Nanda, J.; Wolfenstine, J.; Sakamoto, J. Controlling and correlating the effect of grain size with the mechanical and electrochemical properties of $Li_7La_3Zr_2O_{12}$ solid-state electrolyte. *J. Mater. Chem. A* **2017**, *5*, 21491–21504. [CrossRef]
32. Matsuki, Y.; Noi, K.; Deguchi, M.; Sakuda, A.; Hayashi, A.; Tatsumisago, M. Lithium dissolution/deposition behavior of Al-doped $Li_7La_3Zr_2O_{12}$ ceramics with different grain sizes. *J. Electrochem. Soc.* **2019**, *166*, A5470. [CrossRef]
33. Basappa, R.H.; Ito, T.; Morimura, T.; Bekarevich, R.; Mitsuishi, K.; Yamada, H. Grain boundary modification to suppress lithium penetration through garnet-type solid electrolyte. *J. Power Sources* **2017**, *363*, 145–152. [CrossRef]
34. Xu, B.; Li, W.; Duan, H.; Wang, H.; Guo, Y.; Li, H.; Liu, H. Li_3PO_4 -added garnet-type $Li_{6.5}La_3Zr_{1.5}Ta_{0.5}O_{12}$ for Li-dendrite suppression. *J. Power Sources* **2017**, *354*, 68–73. [CrossRef]
35. Hosokawa, H.; Takeda, A.; Inada, R.; Sakurai, Y. Tolerance for Li dendrite penetration in Ta-doped $Li_7La_3Zr_2O_{12}$ solid electrolytes sintered with $Li_{2.3}C_{0.7}B_{0.3}O_3$ additive. *Mater. Lett.* **2020**, *279*, 128481. [CrossRef]
36. Hong, M.; Dong, Q.; Xie, H.; Clifford, B.C.; Qian, J.; Wang, X.; Luo, J.; Hu, L. Ultrafast sintering of solid-state electrolytes with volatile fillers. *ACS Energy Lett.* **2021**, *6*, 3753–3760. [CrossRef]
37. Guo, H.; Su, J.; Zha, W.; Xiu, T.; Song, Z.; Badding, M.E.; Jin, J.; Wen, Z. Achieving high critical current density in Ta-doped $Li_7La_3Zr_2O_{12}/MgO$ composite electrolytes. *J. Alloys Compd.* **2021**, *856*, 157222. [CrossRef]
38. Zheng, C.; Ruan, Y.; Su, J.; Song, Z.; Xiu, T.; Jin, J.; Badding, M.E.; Wen, Z. Grain boundary modification in garnet electrolyte to suppress lithium dendrite growth. *Chem. Eng. J.* **2021**, *411*, 128508.
39. Hitz, G.T.; McOwen, D.M.; Zhang, L.; Ma, Z.; Fu, Z.; Wen, Y.; Gong, Y.; Dai, J.; Hamann, T.R.; Hu, L.; et al. High-rate lithium cycling in a scalable trilayer Li-garnet-electrolyte architecture. *Mater. Today* **2019**, *22*, 50–57. [CrossRef]
40. Huo, H.; Liang, J.; Zhao, N.; Li, X.; Lin, X.; Zhao, Y.; Adair, K.; Li, R.; Guo, X.; Sun, X. Dynamics of the garnet/Li interface for dendrite-free solid-state batteries. *ACS Energy Lett.* **2020**, *5*, 2156–2164. [CrossRef]
41. Koshikawa, H.; Matsuda, S.; Kamiya, K.; Miyayama, M.; Kubo, Y.; Uosaki, K.; Hashimoto, K.; Nakanishi, S. Electrochemical impedance analysis of the Li/Au- $Li_7La_3Zr_2O_{12}$ interface during Li dissolution/deposition cycles: Effect of pre-coating $Li_7La_3Zr_2O_{12}$ with Au. *J. Electroanal. Chem.* **2019**, *835*, 143–149. [CrossRef]
42. Wang, M.; Wolfenstine, J.; Sakamoto, J. Temperature dependent flux balance of the Li/ $Li_7La_3Zr_2O_{12}$ interface. *Electrochim. Acta* **2019**, *296*, 842–847. [CrossRef]
43. Wang, M.; Choudhury, R.; Sakamoto, J. Characterizing the Li-solid-electrolyte interface dynamics as a function of stack pressure and current density. *Joule* **2019**, *3*, 2165–2178. [CrossRef]
44. Krauskopf, T.; Mogwitz, B.; Hartmann, H.; Singh, D.K.; Zeier, W.G.; Janek, J. The fast charge transfer kinetics of the lithium metal anode on the garnet-type solid electrolyte $Li_{6.25}Al_{0.25}La_3Zr_2O_{12}$. *Adv. Energy Mater.* **2020**, *10*, 2000945. [CrossRef]
45. Liu, X.; Garcia-Mendez, R.; Lupini, A.R.; Cheng, Y.; Hood, Z.D.; Han, F.; Sharafi, A.; Idrobo, J.C.; Dudney, N.J.; Wang, C.; et al. Local electronic structure variation resulting in Li ‘filament’ formation within solid electrolytes. *Nat. Mater.* **2021**, *20*, 1485–1490.
46. Cao, D.; Sun, X.; Li, Q.; Natan, A.; Xiang, P.; Zhu, H. Lithium dendrite in all-solid-state batteries: Growth mechanisms, suppression strategies, and characterizations. *Matter* **2020**, *3*, 57–94. [CrossRef]
47. Lu, Y.; Zhao, C.-Z.; Yuan, H.; Cheng, X.-B.; Huang, J.-Q.; Zhang, Q. Critical current density in solid-state lithium metal batteries: Mechanism, influences, and strategies. *Adv. Funct. Mater.* **2021**, *31*, 2009925. [CrossRef]
48. Sarkar, S.; Thangadurai, V. Critical current densities for high-performance all-solid-state Li-metal batteries: Fundamentals, mechanisms, interfaces, materials, and applications. *ACS Energy Lett.* **2022**, *7*, 1492–1527. [CrossRef]
49. Matsuda, Y.; Sakaida, A.; Sugimoto, K.; Mori, D.; Takeda, Y.; Yamamoto, O.; Imanishi, N. Sintering behavior and electrochemical properties of garnet-like lithium conductor $Li_{6.25}M_{0.25}La_3Zr_2O_{12}$ (M : Al^{3+} and Ga^{3+}). *Solid State Ion.* **2017**, *311*, 69–74. [CrossRef]
50. Inada, R.; Takeda, A.; Yamazaki, Y.; Miyake, S.; Sakurai, Y.; Thangadurai, V. Effect of postannealing on the properties of a Ta-doped $Li_7La_3Zr_2O_{12}$ solid electrolyte degraded by Li dendrite penetration. *ACS Appl. Energy Mater.* **2020**, *3*, 12517–12524. [CrossRef]
51. Awaka, J.; Takashima, A.; Kataoka, K.; Kijima, N.; Idemoto, Y.; Akimoto, J. Crystal structure of fast lithium-ion-conducting cubic $Li_7La_3Zr_2O_{12}$. *Chem. Lett.* **2011**, *40*, 60–62. [CrossRef]
52. Wakasugi, J.; Munakata, H.; Kanamura, K. Improvement of sintering of $Li_{6.25}Al_{0.25}La_3Zr_2O_{12}$ by using pre-heat treatment. *Solid. State Ion.* **2017**, *309*, 9–14. [CrossRef]
53. Allen, J.L.; Wolfenstein, J.; Rangasamy, E.; Sakamoto, J. Effect of substitution (Ta, Al, Ga) on the conductivity of $Li_7La_3Zr_2O_{12}$. *J. Power Sources* **2012**, *206*, 315–319. [CrossRef]
54. Eckhardt, J.K.; Klar, P.J.; Janek, J.; Heiliger, C. Interplay of dynamic constriction and interface morphology between reversible metal anode and solid electrolyte in solid state batteries. *ACS Appl. Mater. Interface* **2022**, *14*, 33545–33554. [CrossRef] [PubMed]